Article

High-speed, phase-dominant spatial light modulation with silicon-based active resonant antennas

Yu Horie, Amir Arbabi, Ehsan Arbabi, Seyedeh Mahsa Kamali, and Andrei Faraon

ACS Photonics, **Just Accepted Manuscript** • DOI: 10.1021/acsphotonics.7b01073 • Publication Date (Web): 08 Nov 2017

High-speed, phase-dominant spatial light modulation with silicon-based active resonant antennas

Yu Horie,[†] Amir Arbabi,[†,‡] Ehsan Arbabi,[†] Seyedeh Mahsa Kamali,[†] and Andrei Faraon[*,†,¶]

[†]*T. J. Watson Laboratory of Applied Physics, California Institute of Technology, 1200 E California Blvd, Pasadena, CA 91125, USA*

[‡]*Present address: Department of Electrical and Computer Engineering, University of Massachusetts, 151 Holdsworth Way, Amherst, MA 01003, USA.*

E-mail: faraon@caltech.edu

Abstract

Spatiotemporal control of optical wavefronts is of great importance in numerous free-space optical applications including imaging in 3D and through scattering media, remote sensing, and generation of various beam profiles for microscopy. Progress in these applications is currently limited due to lack of compact and high-speed spatial light modulators. Here we report an active antenna comprising a free-space coupled asymmetric Fabry–Perot resonator, that produces a phase-dominant thermo-optic modulation of reflected light at frequencies approaching tens of kilohertz. As a proof of concept for spatial light modulation, we demonstrate a 6×6 array of such active antennas with beam deflection capability. The robust design of our silicon-based active antenna will enable large-scale integration of high-speed, phase-dominant spatial light modulators.

Keywords

subwavelength grating; diffractive optical element; high-index contrast; spatial light modulator; silicon photonics

A spatial light modulator (SLM) is an optoelectronic device that imposes a spatially varying modulation on a beam of light.[1] Particularly, spatiotemporal control of the wavefront (i.e., phase) of light is of great importance for a wide range of applications including beam steering, imaging, holography, optical tweezers, and remote sensing. However, the absence of compact and inexpensive SLMs that can freely modulate the wavefront of light at a high speed is hindering the widespread adoption of popular technologies such as LiDAR (light detection and ranging)[2] and *in-vivo* wavefront correction in biomedical imaging.[3] The liquid crystal on silicon is the most mature technology used for SLMs, that showcases several advantages such as no moving parts, low power consumption, and established manufacturing processes.[4] Nonetheless, nematic liquid crystals, which are most commonly used, suffer from a slow response time of tens to hundreds of milliseconds. Ferroelectric liquid crystals show sub-milliseconds response time, but operate only in a binary phase modulation owing to the bistable nature of the material.[5] Stressed liquid crystals can provide a sub-millisecond control with continuous phase modulation;[6] however, their mass production is not feasible due to the requirement of delicate mechanical shearing process. Micro-electro-mechanical systems (MEMS) based movable micro-mirrors, known as digital micro-mirror device (DMD) technology,[7] offer faster spatial light modulation typically at 10 kHz.[8] However, they only operate in a binary amplitude mode resulting from sophisticated device structures, and complex fabrication processes make them less attractive for mass-production. Recently, MEMS-based tunable all-pass filters that use light-weight high-contrast subwavelength grating (SWG) reflectors in a Gires–Tournois interferometer configuration[9] have been demonstrated. The low mass of the SWG reflectors has increased the modulation speed of these devices to over 500 kHz.

In this paper, we demonstrate a high-speed silicon-based active resonant antenna involving no

moving parts, as a basic device element for phase-dominant spatial light modulation. The individual silicon antenna, made of an asymmetric Fabry–Perot resonator formed by a silicon SWG reflector and a distributed Bragg reflector (DBR) exhibits nearly 2π phase-dominant modulation with speed as fast as tens of kHz by means of the silicon's thermo-optic effect at telecom wavelengths. As a proof of concept for spatial light modulation, a 6×6 array of such antennas is actively controlled, yielding a phased array beam deflection capability.

The spatial light modulation scheme composed of silicon-based active antenna array is illustrated in **Figure 1**a, in which each antenna has an independent electrical control over the phase of the reflected light. The individual optical antenna comprises an asymmetric Fabry–Perot resonator[10–12] (**Figure 1**b), whose amplitude and phase response with respect to the laser frequency can be described with the temporal coupled-mode theory.[13] The temporal response of the optical resonator, coupled to a free-space propagating mode by a partially transmitting top mirror, can be modeled by

$$\frac{\mathrm{d}a_\mathrm{c}}{\mathrm{d}t} = j\omega_0 a_\mathrm{c} - \frac{\kappa}{2}a_\mathrm{c} + \sqrt{\kappa_\mathrm{e}}s^+, \tag{1}$$

where a_c is the normalized electric field amplitude of the resonator mode, ω_0 is the resonance frequency, κ is the total energy decay rate of the resonator, and s^+ is the amplitude of the forward propagating free-space mode. The energy decay from the optical resonator has two channels: κ_i and κ_e corresponding to intrinsic loss and coupling rate, respectively, such that $\kappa = \kappa_\mathrm{i} + \kappa_\mathrm{e}$. The amplitude of the backward propagating mode s^- is

$$s^- = -s^+ + \sqrt{\kappa_\mathrm{e}}a_\mathrm{c}. \tag{2}$$

When driving the system with a continuous-wave laser, whose frequency is ω, we can calculate the reflection coefficient spectrum $r(\Delta)$ of the resonant system:

$$r(\Delta) \equiv \frac{s^-}{s^+} = \frac{-j\Delta + \frac{\kappa_\mathrm{e}}{2} - \frac{\kappa_\mathrm{i}}{2}}{j\Delta + \frac{\kappa_\mathrm{e}}{2} + \frac{\kappa_\mathrm{i}}{2}}, \tag{3}$$

where Δ is the frequency detuning defined as $\Delta \equiv \omega - \omega_0$. **Figure 1**c shows the reflectivity and phase as a function of frequency detuning Δ, normalized to κ in two cases; over-coupled ($\kappa_\mathrm{e} > \kappa_\mathrm{i}$) and under-coupled ($\kappa_\mathrm{e} < \kappa_\mathrm{i}$) conditions. The reflection phase spectrum exhibits a nearly 2π rapid phase shift around the resonance frequency only when the resonator is over-coupled, whereas the phase shift is very small in the case of an under-coupled resonator. If the resonance frequency of the over-coupled resonator is tuned by some means, the modulation of the resonance frequency will manifest itself as a phase-dominant modulation of the reflected light. The maximum loss in reflection occurs at an on-resonance frequency ($\Delta = 0$), and can be minimized when $\kappa_\mathrm{e}/\kappa_\mathrm{i} \gg 1$.

To implement such a phase-modulation scheme, we designed a free-space coupled Fabry–Perot resonator comprising a high-contrast SWG reflector[14–18] made of high-index amorphous silicon (α-Si) bars on a DBR made of a quarter-wave stack of silicon nitride (SiN_x) and silicon dioxide (SiO_2) spaced by an SiO_2 cavity layer as depicted in **Figure 1**d. SWG reflectors integrated in Fabry-Perot resonators have also been used to realize vertical-cavity surface-emitting lasers (VCSELs)[19] by replacing the conventional DBRs, and also to show novel MEMS devices.[9,20] This asymmetric Fabry–Perot resonator is equivalent to a conventional Gires–Tournois interferometer, with a bottom mirror exhibiting nearly unity reflectivity and a less reflective top mirror, that is widely used for pulse compression bacause of its highly dispersive phase response. Owing to the high electric field energy density in the silicon SWG layer when used in a Fabry–Perot resonator[21] (**Figure 1**d), the resonance frequency can be efficiently tuned with respect to the wavelength of the incident light by modulating the refractive index of the silicon bars. The large thermo-optic coefficient of α-Si ($\mathrm{d}n/\mathrm{d}T \approx 2 \times 10^{-4}\,/\mathrm{K}$)[22] can be practically used by integrating a microheater around the device, but far enough from the area of the optical resonator to avoid optical absorption loss. **Figure 1**e shows the simulated phase modulation as well as the reflectivity change for a TM-polarized (i.e., electric field perpendicular to the grating bars) normally incident light as a function of the temperature change in the α-Si bars resulting in the refractive index modulation of α-Si. Using the temporal coupled-mode theory results, the coupling rate κ_e is related to the reflection coefficient of the top SWG reflector. The intrinsic decay rate κ_i accounts for the losses of the resonator such as

transmission through the bottom reflector, scattering loss due to the surface roughness, and lateral energy leakage due to the finite extent of the optical mode. It should be noted again that nearly 2π phase modulation is achieved under the over-coupled resonator condition $\kappa_{\mathrm{e}} > \kappa_{\mathrm{i}}$ (i.e., coupling rate of the antenna to the free-space mode has to be greater than the total intrinsic decay rate).

To experimentally verify our phase modulation scheme, we fabricated and tested the designed silicon antenna structure. A scanning electron microscope (SEM) image of a single element of the device with the integrated microheater made of nichrome (NiCr) is shown in **Figure 2**a. We measured the reflectivity spectra of the fabricated antenna for a normally incident TM-polarized beam using a custom-built confocal microscope setup by scanning a tunable laser (see **Figure S1** in Supporting Information for the detailed measurement setup) as shown in **Figure 2**b. By fitting the reflectivity spectra with 3, we found that the measured loaded quality factor (Q-factor; $Q \equiv \omega_0/\kappa$) of the resonance was around 1.9×10^2 (the intrinsic Q-factor was around 1.1×10^3) at 1525 nm and the maximum loss at resonance was approximately 58%. The over-coupled condition ($\kappa_{\mathrm{e}} > \kappa_{\mathrm{i}} \Leftrightarrow Q_{\mathrm{e}} < Q_{\mathrm{i}}$) was determined by the phase measurement later on. Passing a DC current through the integrated microheater, we confirmed the resonance wavelength tunability owing to the thermo-optic effect of α-Si without degrading the optical resonance. **Figure 2**c shows the resonance wavelength shift as a function of the electrical power injected into the NiCr microheater with measured resistance of $\sim 7.2 \times 10^3\ \Omega$, indicating a tuning rate of about 0.77 nm/mW, benefiting from the high thermo-optic coefficient of silicon. Next, we measured the reflected phase using a cross-polarization setup, in which the phase of the reflected TM-polarized beam of interest was extracted by interfering it with a co-propagating TE-polarized beam, which does not couple to the antenna (see **Figure S2** in Supporting Information). After fitting the measured intensities with a theoretical model, the reflected phase curves were computed as shown in **Figure 2**b. A phase change $\sim 1.6\pi$ across the resonance wavelength was observed, implying the resonance was over-coupled ($\kappa_{\mathrm{e}} > \kappa_{\mathrm{i}}$) as we intended. The required electrical power to introduce π phase change P_π was 3.5 mW. We also investigated the response times of the phase modulation as shown in **Figure 2**d when a 1 kHz square-wave electrical signal modulated the antenna with P_π. Rise and fall

response times of 74 µs and 66 µs were observed, which are in good agreement with the simulated values (see **Figure S3** in Supporting Information for the simulated response times). The response time is defined as the time duration by which the change in the normalized optical power rises (or falls) from 10% to 90% (or vice versa) from the steady-state when an input signal modulates the microheater.

As a proof of concept for spatial light modulation, a 6×6 array of active silicon antennas was fabricated (**Figure 3**a). The pixel pitch of the array is 26 µm, and the pixel size of the antenna is 20 µm, leading to the fill factor of $\sim 59\%$. The microheaters around the silicon antennas were grouped in every other column and addressed by a single input voltage (to simplify the electrical interconnection), such that the entire phased array displays an alternating phase pattern between the neighboring pixels. Each of the fabricated antennas in the array exhibits a small detuning from the target wavelength, with a standard deviation of 0.44 nm, significantly less than the resonance bandwidth. **Figure 3**b shows the simulated temperature distribution of the device surface when only the central pixel is active, indicating that the designed microheaters can individually address the pixels. A thermal crosstalk of 8% is measured by the temperature change in the center of the neighboring pixels. The far-field patterns of the phased array were measured by imaging the back focal plane of an objective lens placed after the phased array. The intended phase patterns of the phased array are shown in **Figure 3**c, illuminated with a collimated beam whose profile has a Gaussian beam waist of 75 µm. This results in deflecting part of the incident beam to ± 1st orders as shown in **Figure 3**d. A strong diffraction pattern is seen in the far-field when no voltage is applied ("off" state), because the filling factor of the phased array is smaller than unity. When the voltage was tuned to introduce a π phase shift in every column ("on" state; electrical power $P = 18P_\pi$ was applied, where half of 36 pixels are addressed), the phased array beam deflection was observed at the angle given by $\theta_{\max} = \sin^{-1}(\lambda/2p) \approx 1.7^\circ$, where λ is the wavelength of the light and p is the pixel pitch of the phased array. **Figure 3**e shows the 1D profiles along the deflection direction of the measured far-field patterns that are in good agreement with the simulated ones, confirming the robustness of the proposed device design. The beam deflection efficiency, measured as the ratio

between the total of ± 1st order deflected beams and that of the undiffracted zeroth order beam, was about 40% at best, which is not possible through amplitude-only modulation (see **Figure S4** in Supporting Information).

The demonstrated response time in phase modulation is currently dominated by the large thermal resistance between the α-Si SWG layer and the silicon substrate, owing to the low thermal conductivities of the $\sim$6-μm-thick DBR layers. Substituting the material for a good thermal conductor (e.g. polycrystalline silicon or GaAs/AlGaAs-based DBR) or thinning the DBR layers should greatly improve the response time.[23] As a point of reference, sub-microseconds response was reported by means of direct heating of silicon waveguides in the context of an on-chip Mach–Zehnder interferometer, where the buried oxide layer in a silicon-on-insulator substrate was 1 μm.[24] Even further improvement of the modulation speed up to hundreds of MHz can be expected by deploying the same device design but with a p-i-n diode structure along the silicon bars and using the plasma dispersion effect[25–27] or the Kerr effect.[28] However, in this case, one would need an optical resonance with much higher Q-factor, as those modulation methods can practically achieve a refractive index change on the order of 10^{-4}, an order of magnitude smaller than the one achievable via the thermo-optic effect. While it is beneficial to design an over-coupled resonator with high Q-factor, one would also need to pay more attention to the loss in the resonator. When non-negligible loss is present in the resonator, the change in the amplitude is coupled to the phase-dominant modulation as is the case for our experiments in **Figure 2**b. In general, phase-only spatial light modulation is preferable to the phase-dominant one because the unwanted change in the amplitude contributes to diffraction into undesired orders. It is noteworthy to mention again that the loss can be minimized when $\kappa_{\mathrm{e}}/\kappa_{\mathrm{i}} \gg 1$.

The pixel pitch and the fill factor are also important parameters in spatial light modulation. The former imposes a limit on the maximum spatial frequency or deflection angle,[29] and the latter leads to beam deflection efficiency loss as it contributes to the undiffracted components. In our scheme, if we reduce the size of the antenna, the number of SWG bars in a pixel will be lower, and additional loss will be induced due to the lack of lateral mode confinement.[30] This can be circum-

vented by several approaches including the effective index method[31] and the phase gradient mirror approach,[32] to further shrink the size of the antennas. Alternatively, even without having a smaller pixel pitch, one can think of enlarging the deflection angle limit using appropriate magnification optics to access a larger spatial frequency. The proposed phased array scheme can be immediately extended to use advanced electrical circuitry schemes such as an active matrix addressing to independently control the enormous number of pixels or vertical integration of wiring layers to maximize the fill factor of the pixels. Furthermore, the presented modulation scheme is applicable over the entire near-infrared spectrum with the proper scaling for the device dimensions, because the α-Si that was used to form the SWG reflector as well as other materials is transparent above the wavelength of 700 nm.[33]

In summary, we demonstrated a silicon-based active antenna based on an over-coupled optical resonator system, where the phase modulation for the light propagating in free space is achieved via the refractive index modulation of silicon. The fabricated active antenna exhibits phase-dominant thermo-optic modulation with a response time of $\sim$70 µs, an order of magnitudes faster than the conventional liquid crystal based SLMs. A phased array beam deflection was demonstrated with a 6×6 array of such active antennas. The demonstrated design can be easily integrated in a scalable fashion using conventional CMOS technology (e.g. silicon photonics[34,35]), allowing large-scale phase-dominant SLMs to be implemented on inexpensive and compact photonic chips. As such, the presented spatial light modulation device will enable cost-effective beam steering solutions for LiDAR and scanning microscopy.

Methods

Device Fabrication.

For silicon-based active antenna fabrication, we started with a 675-µm-thick silicon substrate. We deposited the DBR structure with 12 pairs of SiN_x/SiO_2 quarter-wave stacks (195 nm and 258 nm in thicknesses, respectively) at 350°C using the plasma enhanced chemical vapor depo-

sition (PECVD) method. Then, a 415-nm-thick SiO_2 and a 435-nm-thick α-Si:H (hydrogenated amorphous silicon) layer were deposited at 200°C also by PECVD. The top α-Si layer was then patterned by electron beam lithography and dry etched in a mixture of SF_6 and C_4F_8 plasma, to form the top silicon SWG reflector (period: 675 nm, width: 430 nm, height: 435 nm). 100 nm-thick, 1 μm-wide NiCr heaters surrounding the antennas were then patterned using a lift-off process, and subsequently Au contact pads were fabricated.

Measurement Procedure.

For optical measurements, including the reflectivity spectra from single active antennas and far-field patterns, we used a custom-built confocal microscope setup illustrated in **Figure S1** in Supporting Information. A continuous-wave laser light emitted from a tunable external cavity laser diode (Photonetics, TUNICS-Plus) was collimated using a fiber collimation package (Thorlabs, F260FC-1550). A polarizing beamsplitter (PBS), a half waveplate (HWP), and a quarter waveplate (QWP) were inserted to set a desired polarization state of the incident light. The device was illuminated with a beam whose profile has a Gaussian beam waist of 75 μm on the device. The reflected field was imaged by a pair of a $20\times$ infinity-corrected objective lens (Mitutoyo, M Plan Apo NIR) and a tube lens with a focal length of 200 mm onto a pinhole with a diameter of 400 μm to select a region of interest with diameter of 20 μm in the object plane. The spatially filtered light was either focused onto an InGaAs detector (Thorlabs, PDA10CS) for the measurement of the reflectivity spectra by scanning the source wavelength, or imaged on an InGaAs SWIR camera (Goodrich, SU320HX-1.7RT) for both the near-field and the far-field measurements using relay optics. For the measurement of temporal responses, the bias voltages, both DC and AC, were applied with a function generator (Stanford Research System, DS345).

Phase Measurement in a Cross-Polarized Setup.

For the reflection phase measurement, we inserted a QWP and a HWP between the PBS and the antenna (see **Figure S1** in Supporting Information). The waveplates were used to convert the

linearly polarized beam into an elliptically polarized beam with electric-field components parallel and orthogonal to the resonance of the antenna. Only the parallel component (TM-polarization) can acquire a drastic phase shift due to the antenna resonance, while the orthogonal component (co-propagating TE-polarization) does not. The detected light intensities through the PBS are results of interference between those two components:

$$I_{\mathrm{out}}(\lambda, \theta) = |A(\theta)[-r_{\mathrm{c}}(\lambda) + B(\theta, r_0)]|^2, \tag{4}$$

where θ is the QWP angle and the HWP angle is fixed at 22.5° relative to the vertical polarization of the PBS, $A(\theta) = 1 + \cos(4\theta) + 2j\sin(2\theta)$, and $B(\theta, r_0) = r_0\left(\frac{1+\cos(4\theta)-2j\sin(2\theta)}{1+\cos(4\theta)+2j\sin(2\theta)}\right)$. r_{c} and r_0 are the reflection coefficients for TM- and TE-polarized light, respectively. By measuring I_{out} for different θ and fitting the data with the equations, the reflection phase can be determined.

Supporting Information Available

Schematic of experimental setup, measured reflectivity spectra for phase measurements, simulated response times in temperature modulation, and simulated phased array beam deflection.

Acknowledgement

This work was supported by Samsung Electronics and DARPA. The device nanofabrication was performed in the Kavli Nanoscience Institute at California Institute of Technology. Y.H. acknowledges support from a Japan Student Services Organization (JASSO) fellowship.

Author Information

Corresponding Authors

* E-mail:

A.F.: faraon@caltech.edu

Notes

The authors declare no competing financial interest.

References

(1) Efron, U. *Spatial Light Modulator Technology: Materials, Devices and Applications*; Marcel Dekker, 1994.

(2) Schwarz, B. LIDAR: Mapping the world in 3D. *Nat. Photon.* **2010**, *4*, 429–430.

(3) Ntziachristos, V. Going deeper than microscopy: the optical imaging frontier in biology. *Nat. Methods* **2010**, *7*, 603–614.

(4) Zhang, Z.; You, Z.; Chu, D. Fundamentals of phase-only liquid crystal on silicon (LCOS) devices. *Light: Sci. Appl.* **2014**, *3*, e213.

(5) Engström, D.; O'Callaghan, M. J.; Walker, C.; Handschy, M. A. Fast beam steering with a ferroelectric-liquid-crystal optical phased array. *Appl. Opt.* **2009**, *48*, 1721–1726.

(6) Wang, B.; Zhang, G.; Glushchenko, A.; West, J. L.; Bos, P. J.; McManamon, P. F. Stressed liquid-crystal optical phased array for fast tip-tilt wavefront correction. *Appl. Opt.* **2005**, *44*, 7754–7759.

(7) Dudley, D.; Duncan, W. M.; Slaughter, J. Emerging digital micromirror device (DMD) applications. Proc. SPIE. 2003; pp 14–25.

(8) Shrauger, V.; Warde, C. Development of a high-speed high-fill-factor phase-only spatial light modulator. Proc. SPIE. 2001; pp 101–108.

(9) Yang, W.; Sun, T.; Rao, Y.; Megens, M.; Chan, T.; Yoo, B.-W.; Horsley, D. A.; Wu, M. C.; Chang-Hasnain, C. J. High speed optical phased array using high contrast grating all-pass filters. *Opt. Express* **2014**, *22*, 20038–20044.

(10) Yariv, A.; Yeh, P. *Photonics: Optical Electronics in Modern Communications*; Oxford University Press, 2007.

(11) Soref, R. A.; Bennett, B. R. Electro-optic Fabry-Perot pixels for phase-dominant spatial light modulators. *Appl. Opt.* **1992**, *31*, 675–680.

(12) Colburn, S.; Zhan, A.; Majumdar, A. Tunable metasurfaces via subwavelength phase shifters with uniform amplitude. *Sci. Rep.* **2016**, *7*, 40174.

(13) Haus, H. A. *Waves and Fields in Optoelectronics*; Prentice-Hall, 1983.

(14) Mateus, C. F.; Huang, M. C.; Chen, L.; Chang-Hasnain, C. J.; Suzuki, Y. Broad-band mirror (1.12-1.62 μm) using a subwavelength grating. *IEEE Photon. Technol. Lett.* **2004**, *16*, 1676–1678.

(15) Lalanne, P.; Hugonin, J. P.; Chavel, P. Optical properties of deep lamellar gratings: a coupled Bloch-mode insight. *J. Light. Technol.* **2006**, *24*, 2442–2449.

(16) Karagodsky, V.; Sedgwick, F. G.; Chang-Hasnain, C. J. Theoretical analysis of subwavelength high contrast grating reflectors. *Opt. Express* **2010**, *18*, 16973–16988.

(17) Fattal, D.; Li, J.; Peng, Z.; Fiorentino, M.; Beausoleil, R. G. Flat dielectric grating reflectors with focusing abilities. *Nat. Photon.* **2010**, *4*, 466–470.

(18) Chang-Hasnain, C. J.; Yang, W. High-contrast gratings for integrated optoelectronics. *Adv. Opt. Photonics* **2012**, *4*, 379–440.

(19) Huang, M. C.; Zhou, Y.; Chang-Hasnain, C. J. A surface-emitting laser incorporating a high-index-contrast subwavelength grating. *Nat. Photon.* **2007**, *1*, 119–122.

(20) Huang, M. C. Y.; Zhou, Y.; Chang-Hasnain, C. J. A nanoelectromechanical tunable laser. *Nat. Photon.* **2008**, *2*, 180–184.

(21) Zhao, D.; Ma, Z.; Zhou, W. Field penetrations in photonic crystal Fano reflectors. *Opt. Express* **2010**, *18*, 14152–14158.

(22) Frey, B. J.; Leviton, D. B.; Madison, T. J. Temperature-dependent refractive index of silicon and germanium. Proc. SPIE. 2006; p 62732J.

(23) Atabaki, A. H.; Shah Hosseini, E.; Eftekhar, A. A.; Yegnanarayanan, S.; Adibi, A. Optimization of metallic microheaters for high-speed reconfigurable silicon photonics. *Opt. Express* **2010**, *18*, 18312–18323.

(24) Geis, M. W.; Spector, S. J.; Williamson, R. C.; Lyszczarz, T. M. Submicrosecond submilliwatt silicon-on-insulator thermooptic switch. *IEEE Photon. Technol. Lett.* **2004**, *16*, 2514–2516.

(25) Soref, R. A.; Bennett, B. R. Electrooptical effects in silicon. *IEEE J. Quant. Electron.* **1987**, *23*, 123–129.

(26) Reed, G. T.; Mashanovich, G.; Gardes, F. Y.; Thomson, D. J. Silicon optical modulators. *Nat. Photon.* **2010**, *4*, 518–526.

(27) Qiu, C.; Chen, J.; Xia, Y.; Xu, Q. Active dielectric antenna on chip for spatial light modulation. *Sci. Rep.* **2012**, *2*, 855.

(28) Timurdogan, E.; Poulton, C. V.; Byrd, M. J.; Watts, M. R. Electric field-induced second-order nonlinear optical effects in silicon waveguides. *Nat. Photon.* **2017**, *11*, 200–206.

(29) Goodman, J. W. *Introduction to Fourier Optics*; McGraw-Hill, 2004.

(30) Chase, C.; Zhou, Y.; Chang-Hasnain, C. J. Size effect of high contrast gratings in VCSELs. *Opt. Express* **2009**, *17*, 24002–24007.

(31) Sciancalepore, C.; Bakir, B. B.; Letartre, X.; Fedeli, J. M.; Olivier, N.; Bordel, D.; Seassal, C.; Rojo-Romeo, P.; Regreny, P.; Viktorovitch, P. Quasi-3D light confinement in double photonic crystal reflectors VCSELs for CMOS-compatible integration. *J. Lightwave Technol.* **2011**, *29*, 2015–2024.

(32) Li, J.; Fattal, D.; Fiorentino, M.; Beausoleil, R. G. Strong optical confinement between non-periodic flat dielectric gratings. *Phys. Rev. Lett.* **2011**, *106*, 193901.

(33) Arbabi, A.; Arbabi, E.; Horie, Y.; Kamali, S. M.; Faraon, A. Planar metasurface retroreflector. *Nat. Photon.* **2017**, *11*, 415–420.

(34) Soref, R. The past, present, and future of silicon photonics. *IEEE J. Sel. Top. Quant. Electron.* **2006**, *12*, 1678–1687.

(35) Sun, J.; Timurdogan, E.; Yaacobi, A.; Hosseini, E. S.; Watts, M. R. Large-scale nanophotonic phased array. *Nature* **2013**, *493*, 195–199.

(36) Liu, V.; Fan, S. S4: A free electromagnetic solver for layered periodic structures. *Comput. Phys. Commun.* **2012**, *183*, 2233–2244.

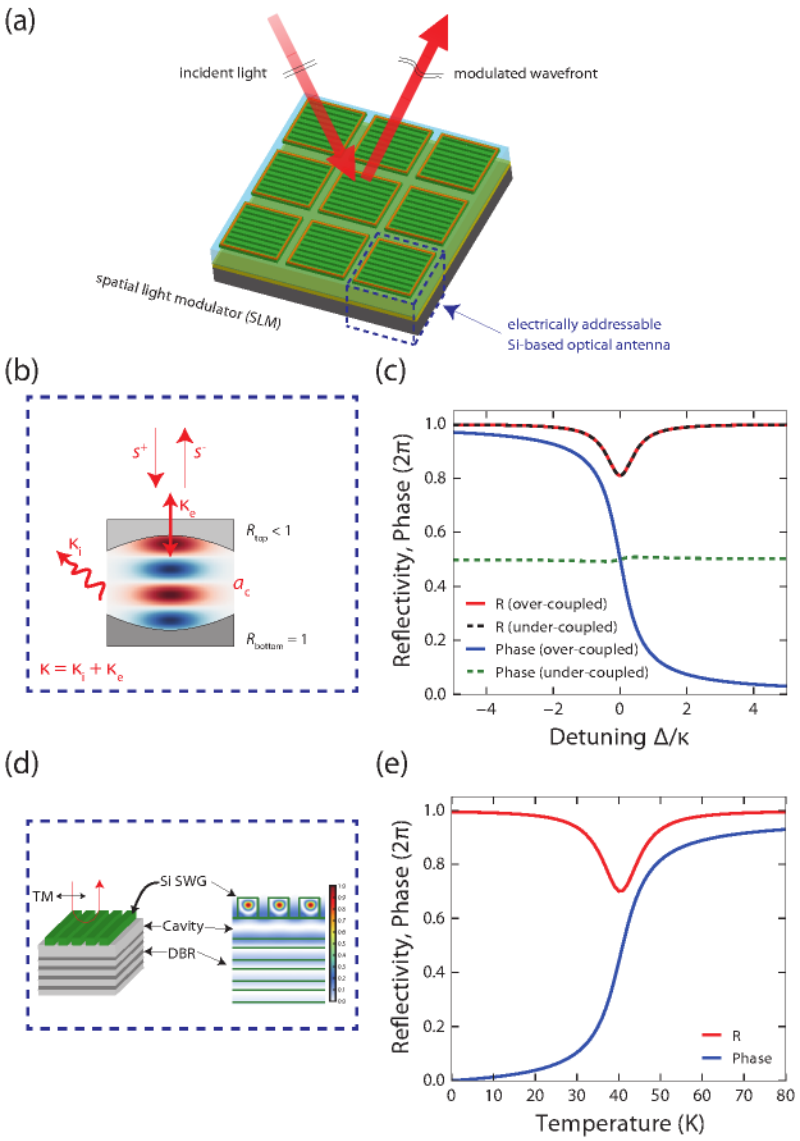

Figure 1: Concept of a phase-dominant spatial light modulator with silicon-based active resonant antennas. (a) Schematic illustration of the SLM, where the active antenna is made of an optical resonator consisting of a silicon SWG layer and a DBR layer. (b) Schematic of the optical resonator. a_c is the normalized electric field amplitude of the resonator mode and ω_0 is the resonance frequency. (c) Reflectivity and phase spectra as a function of frequency detuning Δ, normalized to the total decay rate κ, calculated using the temporal coupled-mode theory. The results for over-coupled ($\kappa_e/\kappa = 0.95$) and under-coupled ($\kappa_e/\kappa = 0.05$) are plotted. (d) Design of the over-coupled resonator realized by a silicon SWG layer on top of a DBR and the normalized magnetic energy density distribution of the corresponding optical resonant mode. (e) Simulated reflectivity change as well as phase response as a function of the temperature variation in the silicon bars, resulting in the refractive index modulation of silicon. The incident is assumed to be a continuous-wave laser light at a wavelength of 1550 nm. The simulation results were calculated by the rigorous coupled wave analysis (RCWA) technique.[36]

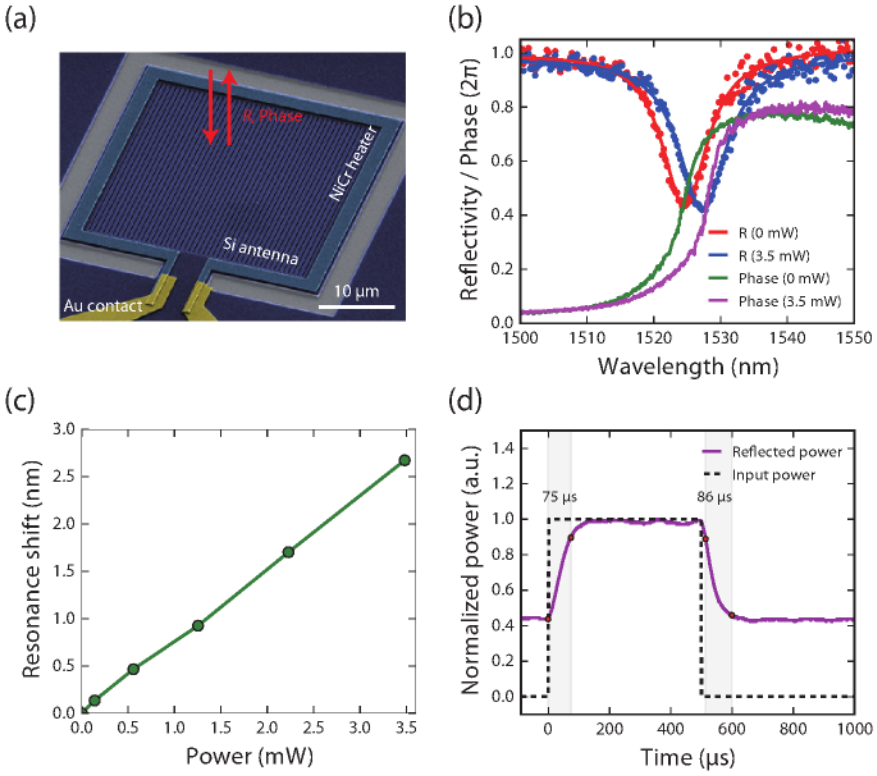

Figure 2: Characterization results of a single active antenna. (a) False-color SEM image of a fabricated single-pixel silicon antenna (pixel size: 20 µm) with a NiCr microheater as well as Au contacts. (b) Measured reflectivity spectra of the antenna and the extracted phase curves. The dispersive phase shift $\sim 1.6\pi$ indicates that the resonance satisfies the over-coupling condition. The required electrical power to introduce π phase shift P_π was found to be 3.5 mW. (c) Measured resonance wavelength tunability by means of silicon's thermo-optic effect, indicating high thermal efficiency of about 0.77 nm/mW. (d) Temporal response of the silicon active antenna, characterized by the modulated optical output power of the reflected light. The measured response time is about 70 µs. The dashed line indicates a 1 kHz square-wave applied across the microheater with an input power of P_π.

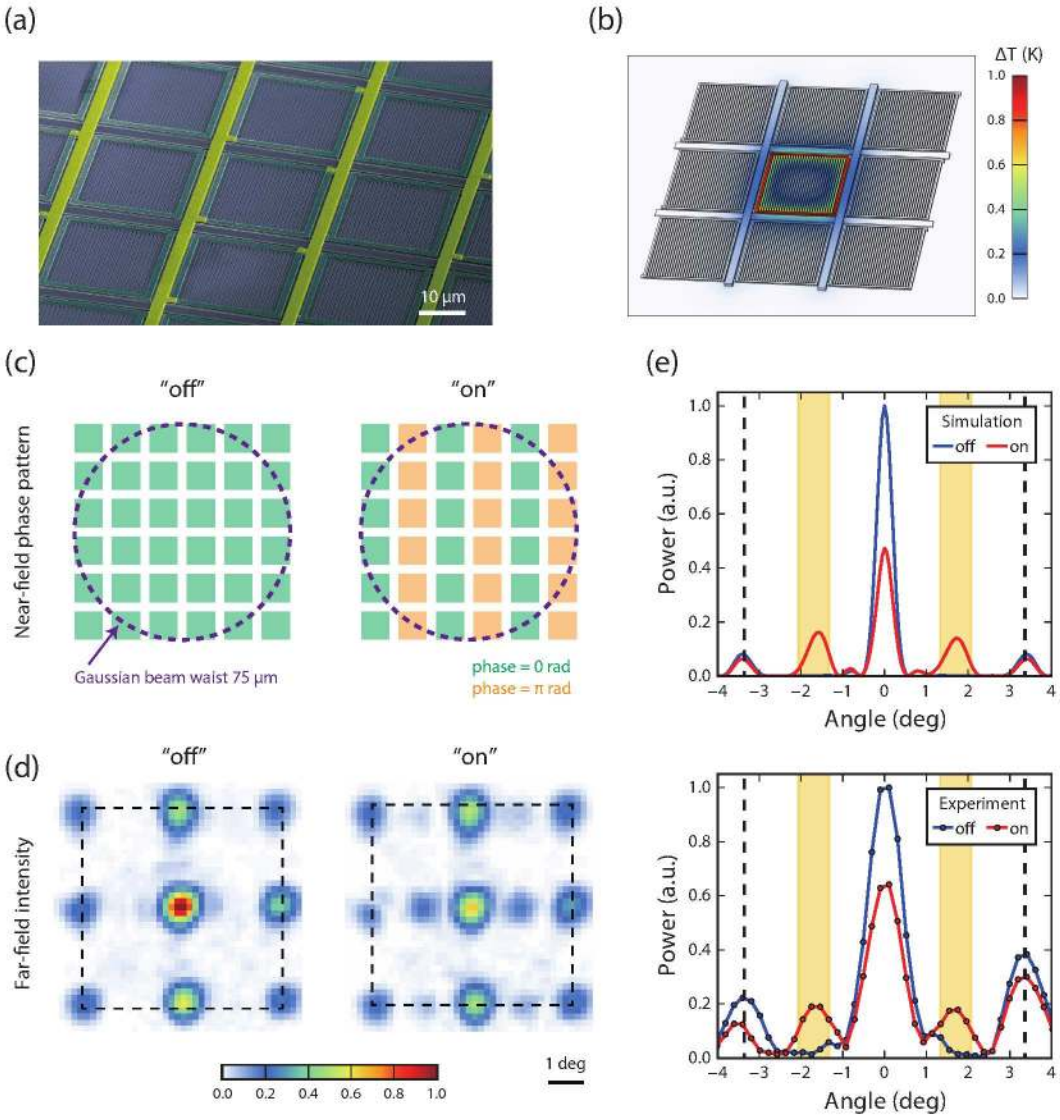

Figure 3: Experimental demonstration of phased array beam deflection. (a) SEM image of the fabricated phased array. (b) Temperature distribution of the surface of the silicon antenna array found using a finite element method (FEM) simulation. (c) Intended near-field phase profile for two states: "off" and "on". The array was illuminated with an incident Gaussian beam profile with a beam waist of 75 μm. (d) Measured far-field patterns for the two states: "off" and "on". The dashed box indicates the ± 1st order diffraction angles imposed by the pixel pitch. (e) Corresponding 1D profiles of the far-field patterns along the deflection direction obtained by simulation (top) and in experiment (bottom). The deflected beam appeared at the angles $\theta = \pm\theta_{\max} = \pm 1.7°$ as denoted by the yellow shades including the Gaussian divergence half angle of $0.37°$. Again, the dashed line corresponds to the angles of the ± 1st diffraction orders.